3D modelling of Self-Amplified X-ray Emission

Edoardo Zavatti, Università Statale degli Studi di Milano, Italy

September 7, 2022

Abstract

In this project we present a theoretical model of interaction between a short wavelenght X-ray beam and a sample of atoms. Exploiting an existent population inversion in the sample, we want to show that the field intensity is enhanced by the interaction with matter. We provide insights on the most relevant theoretical concepts that are needed for the problem and a numerical scheme to solve the equations. Then, we show results of the simulations, comparing them with known analytics and previous simulations.

Contents

Introduction

Since the invention of the first optical laser by Maiman in 1960 [1], people have been trying to create devices that could generate coherent X-ray beams with very short wavelenghts. Indeeed, the shorter the wavelenght, the shorter the pulse duration and the better the imaging. Nowadays, great advances in the field of X-ray free-electron lasers (XFELs) have made it possible to generate hard X-rays (e.g. the energy of the photons is of the order of the kiloelectronvolt) in an angstrom-wavelenght regime.
While traditional lasers usually exploit an inverted population in the atomic levels of matter in order to generate a coherent beam of light, XFELs [2][3][4] use a high energy electron beam as the generating medium. These electons go through an array of magnets arranged one next to the other with opposite polarity, and hence they start to oscillate in space: since electrons are electrically charged particles, these fast accelerations induce the emission of photons in the keV regime. The resulting X-ray beam lasts only a few femtoseconds and have a brightness a billion times greater than the radiation produced by conventional synchrotron light sources[5]. XFELs operate on the principle of self-amplified spontaneous emission (SASE), where the radiation emitted by the electron is further amplified by interaction with the electron beam [5]. This result in intense, short-wavelenght laser bursts that are coherent in a plane transverse to the direction of propagation.
In 2015, Yoneda[6] and his colleagues have demonstrated an atomic X-ray laser that has a well defined wavelenght of $1,54\mathring{A}$, the shortest wavelenght ever, surpassing by a factor 10 an atomic laser that was demonstrated to work at $14,6\mathring{A}$[7]. However, a theoretical model that fully explains the interaction between this laser beam and matter is still missing.
Finally, the aim of this project was to understand a possible theoretical model that describes the propagation and interaction with matter of such a laser beam in three dimensions, and to conduct numerical simulations of these phenomenon. This required the creation of a code to benchmark the results of an already existing code, made by S. Chuchurka, and to produce further simulations. The project was conducted under the supervision of researcher A. Benediktovitch and PhD candidate S. Chuchurka, both working in the FS-TUX group at Desy in Hamburg, whose leader is N. Rohringer.

1 Theoretical insights

1.1 The paraxial wave equation

A fundamental framework for this project has been the paraxial apporximation. Indeed, numerical simulations are, for our purposes, limited to this approximation, which present an analytical solution for the propagation case. In particular, let's first derive the paraxial wave equation: electric fields in free space are governed by the scalar wave equation:

$$[\,\triangle + k^2]E(x, y, z) = 0 \tag{1}$$

where the $\triangle$ symbol corresonds to the Laplacian operator, e.g. $\nabla \cdot \nabla$, and $E(x, y, z)$ is the phasor amplitude of a field that evolves sinusoidally in space; its primary space dependence will then be $\exp(-ikz)$, where k is the wave vector and assuming z as the propagation direction. It is convenient to extract the $\exp(-ikz)$ propagation factor and write the field as follows:

$$E(x, y, z) \coloneqq u(x, y, z) \exp(-ikz) \tag{2}$$

where $u(x, y, z)$ is then the envelope of the field. Rewriting eq. (1) with this decomposition, one gets:

$$\frac{\partial^2 u}{\partial x^2} + \frac{\partial^2 u}{\partial y^2} + \frac{\partial^2 u}{\partial z^2} - 2ik\frac{\partial u}{\partial z} = 0\,. \tag{3}$$

Since the main space dependence in z is represented by the factor $\exp(-ikz)$, the remaining z-dependence is cause by diffraction effects, and will be slow compared to transverse variations[8]. Thus, the second derivative in z can be ignored by performing the *paraxial approximation* :

$$\left|\frac{\partial^2 u}{\partial z^2}\right| \ll \left|2ik\frac{\partial u}{\partial z}\right| \text{ or } \left|\frac{\partial^2 u}{\partial x^2}\right| \text{ or } \left|\frac{\partial^2 u}{\partial y^2}\right|. \tag{4}$$

Rewriting eq. (3) we finally get to the *paraxial wave equation*:

$$\triangle_t u(s,z) - 2ik\frac{\partial u(s,z)}{\partial z} = 0 \tag{5}$$

where $\triangle_t$ represents the Laplacian operator respect to the transverse coordinates $s = (x, y)$ or $s = (r, \theta)$.

1.2 Gaussian beam solution

Equation eq. (5) has an analytical solution, the *gaussian beam*[8]:

$$u(x,y,z) = \sqrt{\frac{2}{\pi}}\frac{\exp(-ikz - i\psi(z)}{w(z)}\exp\Big[-\frac{x^2+y^2}{w^2(z)} - ik\frac{x^2+y^2}{2R(z)}\Big] \tag{6}$$

where $w(z)$ is the beam waist at the plane z, $R(z)$ is the beam radius, $\psi(z)$ is the Guoy phase and z_R is Reyleigh lenght:

$$\begin{aligned} z_R &= \frac{\pi w_0^2}{\lambda} \\ w(z) &= w_0\sqrt{\Big[1 + (\frac{z}{z_R})\Big]} \\ R(z) &= z + \frac{z_R^2}{z} \\ \psi(z) &= \tan^{-1}\big(\frac{z}{z_R}\big). \end{aligned} \tag{7}$$

where w_0 is the beam waist at the source plane and λ is the wavelenght of th efield in the propagation medium.

1.3 Decomposition in Bessel's functions

In the project, we assume the interaction to happen in a 3D cilinder of lenght L and radius R. The light beam was decoupled through Bessel's functions, which represent eigenfunctions of the Laplacian operator. In particular, we consider Bessel's functions $J_k(\mathbf{r})$ as:

$$J_k(\mathbf{r}) := \frac{\tilde{J}_0(\frac{r}{R}\mu_k)}{\sqrt{\pi}R|\tilde{J}_1(\mu_k)|} \tag{8}$$

where $\tilde{J}_0$ and $\tilde{J}_1$ are the usual first and second Bessel's functions, μ_k is the node of order k and $r = \sqrt{x^2+y^2}$ is the usual radial coordinate in the plane. Since our J_k's are all of type 0, we are assuming no angular dependance for the problem, i.e. cilindrical symmetry. Then, if we fix R for the box and an initial waist w_0 for our field, we can decouple the beam $u(r,z)$ of eq. (6) with Bessel's functions. Basically, we need to obtain Bessel's coefficients c_k for the field through a scalar product

$$c_k(z) = \int_0^R \mathrm{d}r\, 2\pi r\, J_k(r)\cdot u(r,z) \tag{9}$$

and then obtain the simulated beam from

$$u(r,z) = \sum_k c_k(z) \cdot J_k(r)\,. \tag{10}$$

Of course if we increase the number of Bessel's function taken into considerations the precision with which we can mimic the shape of the target field improves, as shown in figs. 1 and 2.
Moreover, with our definition of Bessel's functions, expoliting the fact that for usual Bessel's functions stands true that:

$$\begin{aligned} &\int_0^1 \mathrm{d}x\, \tilde{J}_0(x\mu_k) \cdot \tilde{J}_0(x\mu_n) = \delta_{k,n} \\ &\triangle \tilde{J}_0(\frac{r}{R}\mu_k) = -\Big(\frac{\mu_k}{R}\Big)^2 \tilde{J}_0(\frac{r}{R}\mu_k) \end{aligned} \tag{11}$$

then from eq. (11) follows that:

$$\begin{aligned} &\int_0^R \mathrm{d}r\, J_k(r) \cdot J_n(r) = \delta_{k,n} \\ &\int_0^R \mathrm{d}r\, J_k(r)\, \triangle J_n(r) = k_0^2\, K_k\, \delta_{k,n}, \quad K_k = -\frac{\mu_k^2}{R^2 k_0^2} \end{aligned} \tag{12}$$

where k_0 is the wave vector of the field.

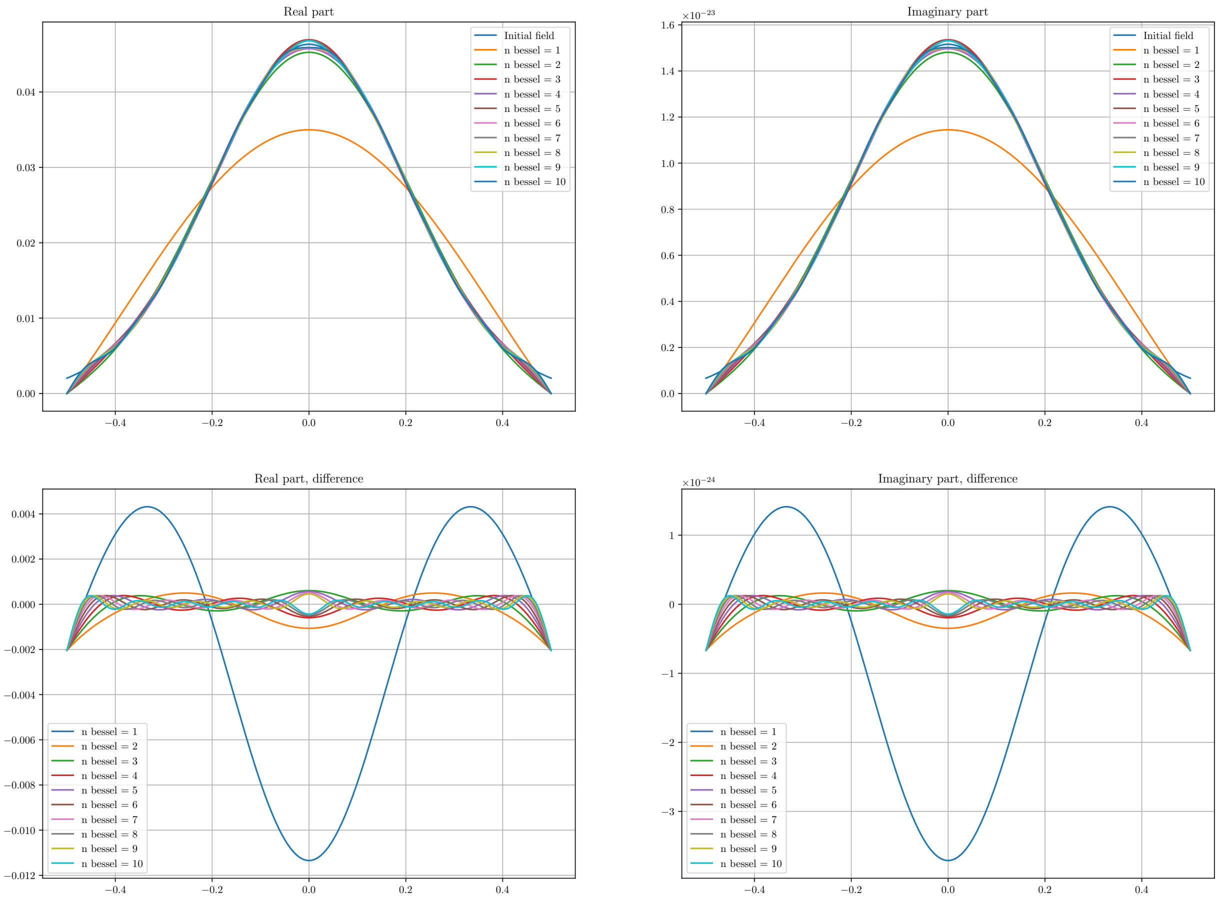

Figure 1: Approaching of the simulated beam to the target beam with increasing number of Bessel's functions for ratio radius of box/beam waist = 2.5. Real (top left) and imaginary (top right) part and difference between the simulated and target beam for the real (bottom left) and imaginary (bottom right) part.

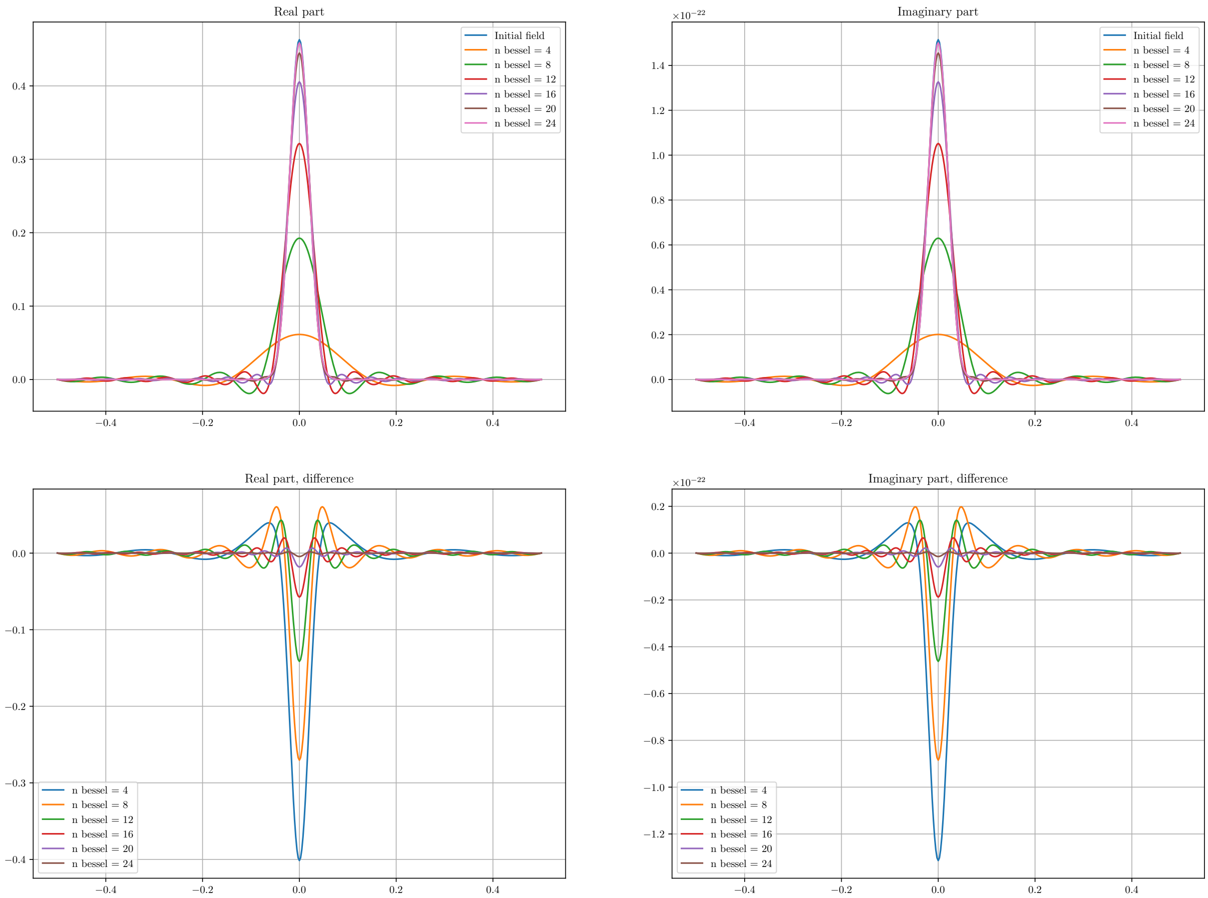

Figure 2: Approaching of the simulated beam to the target beam with increasing number of Bessel's functions for ratio radius of box/beam waist = 25. Real (top left) and imaginary (top right) part and difference between the simulated and target beam for the real (bottom left) and imaginary (bottom right) part.

1.4 Field-matter equations

For our task, we need to solve the Maxwell equations for the electric field in the presence of matter. As a starting point, we can write the field as a sum of field components with positive and negative frequency, i.e.

$$D(\mathbf{r},t) = D^{(+)}(\mathbf{r},t) + D^{(-)}(\mathbf{r},t) \tag{13}$$

Moreover, it is convenient to express the field in terms of Rabi frequency

$$\Omega^{(\pm)}(\mathbf{r},t) = \pm i\frac{d_0 \cdot D^{(\pm)}((\mathbf{r},t)}{\epsilon_0 \hbar}\,, \tag{14}$$

where $\mathbf{d}_0 \equiv \mathbf{d}_{eg}$ is the element (e,g) of the dipole operator matrix $\hat{\mathbf{d}} = -q \cdot \hat{\mathbf{r}}$ for a two level system, q being the elementary charge. In this way, the field has physical units of frequency. The solution in terms of Bessel's components is:

$$\begin{aligned}
\Omega^{(+)}(\mathbf{r},t) &= \sum_k \left(\Omega^{(+)}_{k,>}(z,t)e^{ik_0z} + \Omega^{(+)}_{k,<}(z,t)e^{-ik_0z}\right) e^{-i\omega_0 t}\, J_k(\mathbf{r},t) \\
\Omega^{(-)}(\mathbf{r},t) &= \sum_k \left(\Omega^{(-)}_{k,>}(z,t)e^{ik_0z} + \Omega^{(-)}_{k,<}(z,t)e^{-ik_0z}\right) e^{i\omega_0 t}\, J_k(\mathbf{r},t)
\end{aligned} \tag{15}$$

where $\Omega^{(\pm)}_{k,>}$ represent the k-th Bessel component moving forward, while $\Omega^{(\pm)}_{k,<}$ is the k-th Bessel component moving backward (for positive and negative frequency), and where we have taken out the $\exp(\pm ik_0 z \pm i\omega_0 t)$ dependency of the field, k_0 and ω_0 being the wave vector and the frequency. On the other hand, interaction with matter is modelled through the Maxwell-Bloch equations. In particular, being $\rho(\mathbf{r},t)$ the density martix of the atom at position $\mathbf{r}$ at time t, and neglecting spontaneous decay effects, the equations for the components of the matrix are[9]:

$$\begin{aligned}
\frac{d\rho_{pq}(\mathbf{r},t)}{dt} &= -i(\omega_p - \omega_q)\rho_{pq}(\mathbf{r},t) \\
&\quad + \Omega(\mathbf{r},t)\sum_s \left(\mathbf{d}_{ps}\rho_{sq}(\mathbf{r},t) - \rho_{ps}(\mathbf{r},t)\mathbf{d}_{sq}\right)\,,
\end{aligned} \tag{16}$$

While we are going to solve these equations for the energy levels in real space-time coordinates, it is useful to state that also the density matrix can be expressed in terms of Bessel's functions, just as usual:

$$\begin{aligned}
\rho_{k,pq}(z,t) &= \int_0^R \mathrm{d}r\, 2\pi r\, J_k(r) \cdot \rho_{pq}(z,t) \\
\rho_{pq}(z,t) &= \sum_k \rho_{k,pq}(z,t) \cdot J_k(r)\,.
\end{aligned}$$

Considering a two-level system and applying the rotating wave approximation to eq. (15), one finds the equations for the evolution of the density matrix in real coordinate space:

$$\begin{aligned}\frac{\partial\rho_{ee}(z,t)}{\partial t} =& -\Bigg[\Omega^{(+)}_{>}(z,t)\mathbf{d}_{eg}\rho_{ge}(z,t) + fT\Omega^{(-)}_{>}(z,t)\rho_{eg}(z,t)\mathbf{d}_{ge}+ \\ & + f^{*}T^{*}\Omega^{(+)}_{<}(z,t)\mathbf{d}_{eg}\rho_{ge}(z,t) + \Omega^{(-)}_{<}(z,t)\rho_{eg}(z,t)\mathbf{d}_{ge}\Bigg], \end{aligned} \tag{17}$$

$$\begin{aligned}\frac{\partial\rho_{eg}(z,t)}{\partial t} =& -i(\omega_e-\omega_g)\rho_{eg}(z,t)+ \\ & -\left(\Omega^{(+)}_{>}(z,t) + +f^{*}T^{*}\Omega^{(+)}_{<}(z,t)\right)\left(\mathbf{d}_{eg}\rho_{gg}(z,t) - \rho_{ee}(z,t)\mathbf{d}_{eg}\right), \end{aligned} \tag{18}$$

$$\begin{aligned}\frac{\partial\rho_{ge}(z,t)}{\partial t} =& -i(\omega_e-\omega_g)\rho_{eg}(z,t)+ \\ & +\left(fT\Omega^{(-)}_{>}(z,t) + \Omega^{(-)}_{<}(z,t)\right)\left(\mathbf{d}_{ge}\rho_{ee}(z,t) - \rho_{gg}(z,t)\mathbf{d}_{ge}\right), \end{aligned} \tag{19}$$

$$\begin{aligned}\frac{\partial\rho_{gg}(z,t)}{\partial t} =& \Bigg[fT\Omega^{(-)}_{>}(z,t)\mathbf{d}_{ge}\rho_{eg}(z,t) + \Omega^{(+)}_{>}(z,t)\rho_{ge}(z,t)\mathbf{d}_{eg}+ \\ & + \Omega^{(-)}_{<}(z,t)\mathbf{d}_{ge}\rho_{eg}(z,t) + f^{*}T^{*}\Omega^{(+)}_{<}(z,t)\rho_{ge}(z,t)\mathbf{d}_{eg}\Bigg]. \end{aligned} \tag{20}$$

We note that in our problem we consider $\rho_{eg} = \tilde{\rho}_{eg}\, exp\big[-i(\omega_e-\omega_g)\big]$, so we can forget about the first term in eqs. (18) and (19).
Regarding the field equations, we follow the same path that was illustrated in section 1.1, only this time we are not in vaccum aanymore. We apply once again the paraxial approximation and we use the **retarded time frame**, i.e. we make the following change of variables: $z \to z - ct$, with c the speed of light. Finally, the following set of equations describes the evolution of the Bessel components of the field Ω_k, taking into account the interaction with matter, represented by the Bessel components of the density matrix $\rho_{k,pq}$:

$$\begin{aligned}\frac{\partial\Omega^{(+)}_{k,>}(z,t)}{\partial z} =& i\frac{k_0}{2}\left(K_k\Omega^{(+)}_{k,>}(z,t) + \chi^{(0)}\Omega^{(+)}_{k,>}(z,t) + \chi^{(-)}\Omega^{(+)}_{k,<}(z,t)\right)+ \\ & + \frac{3\lambda_0^2}{8\pi}n\Gamma_{sp}\, d_{ge}\cdot\rho_{k,eg}(z,t)\,, \end{aligned} \tag{21}$$

$$\begin{aligned}-\frac{\partial\Omega^{(+)}_{k,<}(z,t)}{\partial z} + 2\frac{\partial\Omega^{(+)}_{k,<}(z,t)}{c\,\partial t} =& i\frac{k_0}{2}\left(K_k\Omega^{(+)}_{k,<}(z,t) + \chi^{(0)}\Omega^{(+)}_{k,<}(z,t) + \chi^{(+)}\Omega^{(+)}_{k,>}(z,t)\right)+ \\ & + \frac{3\lambda_0^2}{8\pi}n\Gamma_{sp}\, d_{ge}\cdot\rho_{k,eg}(z,t)\,, \end{aligned} \tag{22}$$

$$\frac{\partial \Omega^{(-)}_{k,>}(z,t)}{\partial z} = -i\frac{k_0}{2}\left(K_k\Omega^{(-)}_{k,>}(z,t) + \chi^{(0)*}\Omega^{(-)}_{k,>}(z,t) + \chi^{(-)*}\Omega^{(-)}_{k,<}(z,t)\right) + \\ + \frac{3\lambda_0^2}{8\pi} n\Gamma_{sp}\, d_{eg}\cdot \rho_{k,ge}(z,t)\,, \tag{23}$$

$$\frac{\partial \Omega^{(-)}_{k,<}(z,t)}{\partial z} - 2\frac{\partial \Omega^{(-)}_{k,<}(z,t)}{c\,\partial t} = i\frac{k_0}{2}\left(K_k\Omega^{(-)}_{k,<}(z,t) + \chi^{(0)*}\Omega^{(-)}_{k,<}(z,t) + \chi^{(+)*}\Omega^{(-)}_{k,>}(z,t)\right) + \\ - \frac{3\lambda_0^2}{8\pi} n\Gamma_{sp}\, d_{eg}\cdot \rho_{k,ge}(z,t)\,. \tag{24}$$

We note that n is the atomic density, Γ_{sp} is the spotaneous decay constant and the χ's are the susceptibilities of the medium.

2 Simulations

2.1 Forward propagation

As a firts step in the project we checked if this method of decomposition into Bessel functions could efficiently simulate the propagation of the beam. So, we limited ourself to the propagation in vacuum of the forward propagating wave. The equation taken into account was:

$$\frac{\partial \Omega^{(+)}_{k,>}(z)}{\partial z} = i\frac{k_0}{2}\left(K_k\Omega^{(+)}_{k,>}(z)\right), \tag{25}$$

which is just the first part of eq. (21). For this equation there is a known analytical solution[8], i.e. the gaussian beam solution decribed in section 1.2. All we have to do is solve eq. (25) for each Bessel component k and then recover the field by summing over all k's the product of $\Omega^{(+)}_{k,>}(z)$ with $J_k(r,z)$. In figs. 3 and 4 we show the result of the simulation and the known Gaussian solution for both the module and the phase, and we compare the two simulations. One can see that the difference between the two beams is everywhere in space compatible with zero.

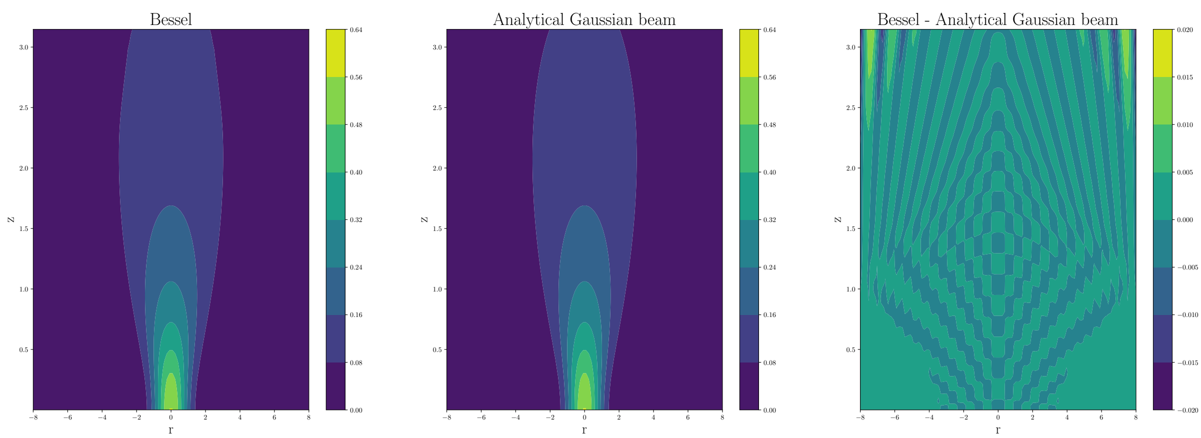

Figure 3: Module of simulated field (left), of the analytical solution (centre), and difference between the two (left).

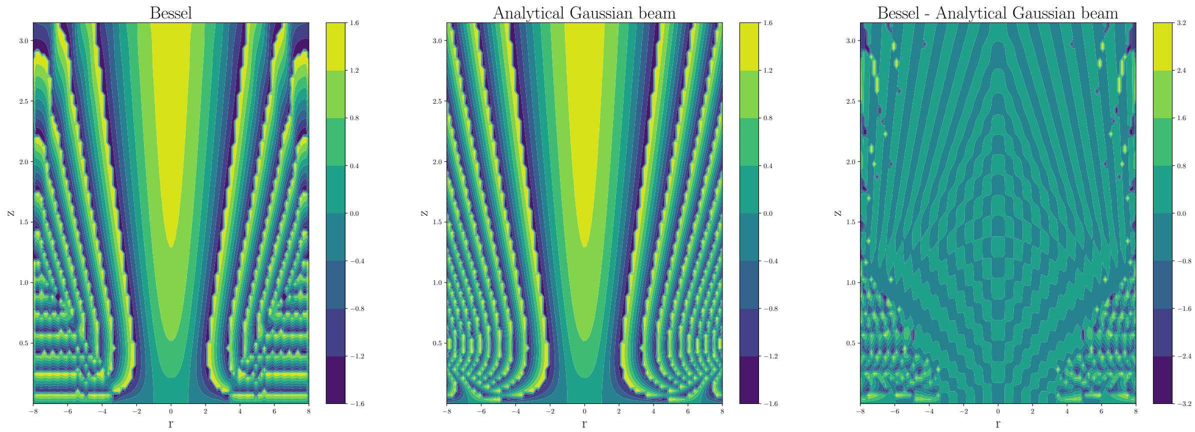

Figure 4: Phase of simulated field (left), of the analytical solution (centre), and difference between the two (left).

2.2 Forward and backward propagation

As a next step, we added the simulatoin of the backward propagating wave, i.e. the $\Omega_{k,<}$ components. Thus, we needed to numerically solve the following system of coupled equations:

$$
\begin{aligned}
\frac{\partial \Omega^{(+)}_{k,>}(z,t)}{\partial z} &= i\frac{k_0}{2} \left(K_k \Omega^{(+)}_{k,>}(z,t) + \chi^{(0)}\Omega^{(+)}_{k,>}(z,t) + \chi^{(-)}\Omega^{(+)}_{k,<}(z,t) \right), \qquad (26)\\
-\frac{\partial \Omega^{(+)}_{k,<}(z,t)}{\partial z} + 2\frac{\partial \Omega^{(+)}_{k,<}(z,t)}{c\,\partial t} &= i\frac{k_0}{2} \left(K_k \Omega^{(+)}_{k,<}(z,t) + \chi^{(0)}\Omega^{(+)}_{k,<}(z,t) + \chi^{(+)}\Omega^{(+)}_{k,>}(z,t) \right). \qquad (27)
\end{aligned}
$$

We will explain better the scheme for solving these equations in the next section. For now, we limit ourselves to showing results of the simulations. In particular, we compare them with a code written in Julia by S. Chuchurka, and we make sure that they are compatible, as shown in figs. 5 and 6.

2.3 Light-matter interaction

As a final step, we added the interaction between light and matter. To do so, we implemented the full system of eqs. (21), (22), (23) and (24) for the field propagation and the Maxwell-Bloch system of eqs. (17), (18), (19) and (20). Since the equations for the field include partial differential equations, it is useful to describe the numerical scheme that was implemented to solve the system. First of all we set a grid of points in space and time, i.e. a 2D grid of (z,t) points, equally separated in space by Δz and in time by $\Delta t = \frac{2}{c}\Delta z$. The reason for this choice of Δt will become evident in a moment.
For eqs. (21) and (23) nothing special happens, they are ordinary differential equations. We simply interpret the derivative as a finite difference, i.e. $\frac{\partial \Omega^{(+)}_{k,>}(z,t)}{\partial z} \simeq \frac{\Omega^{(+)}_{k,>}(z+\Delta z,t) - \Omega^{(+)}_{k,>}(z,t)}{\Delta z}$ while we interpret the field at point (z,t) as an average, i.e. $\Omega^{(+)}_{k,>}(z,t) \simeq \frac{\Omega^{(+)}_{k,>}(z+\Delta z,t) + \Omega^{(+)}_{k,>}(z,t)}{2}$, and we do the same for the density matrix, $\rho_{pq}(z,t) \simeq \frac{\rho_{pq}(z+\Delta z,t)+\rho_{pq}(z,t)}{2}$. So, given a particular field at point (z,t), the

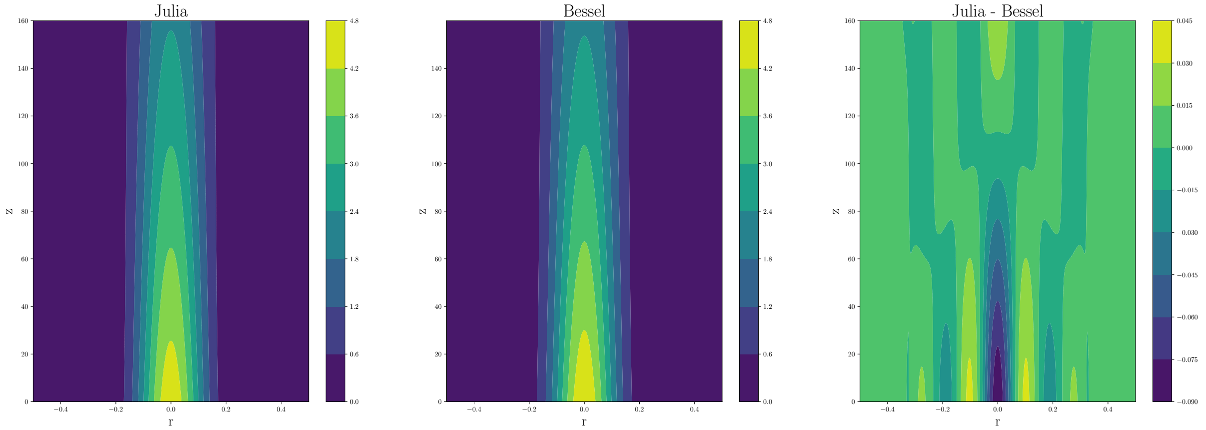

Figure 5: Module of of the simulation of the **forward wave** with the Julia code (left), with the Bessel code simulation (centre), and difference between the two (left).

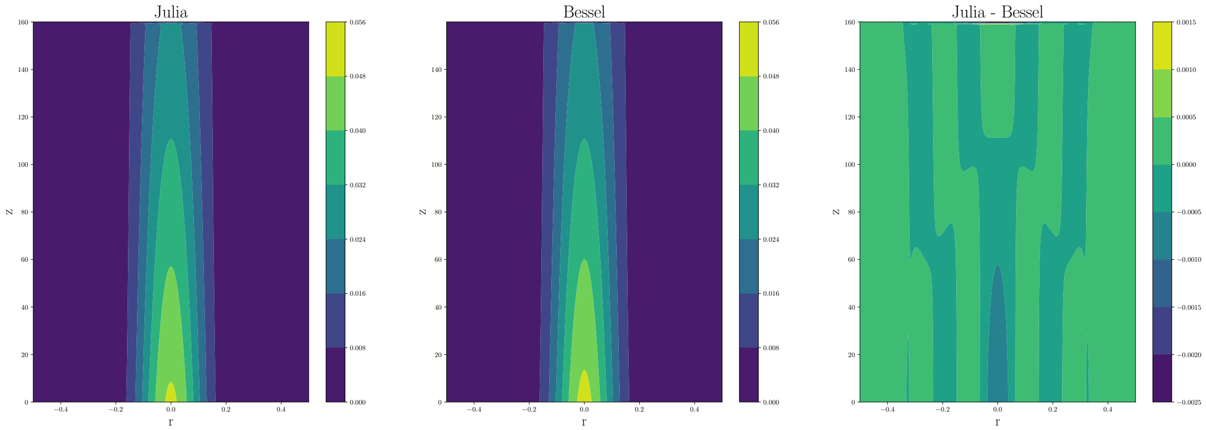

Figure 6: Module of of the simulation of the **backward wave** with the Julia code (left), with the Bessel code simulation (centre), and difference between the two (left).

numerical approximation for $\Omega^{(+)}_{k,>}(z+\Delta z,t)$ is:

$$\begin{aligned}\Omega^{(+)}_{k,>}(z+\Delta z,t) =& \frac{\Omega^{(+)}_{k,>}(z,t)\big[1+i\frac{k_0}{4}\Delta z(K_k+\chi^0)\big]+i\frac{k_0}{4}\chi^{(-)}\Delta z\big[\Omega^{(+)}_{k,<}(z+\Delta z,t)+\Omega^{(+)}_{k,<}(z,t)\big]}{1-i\frac{k_0}{4}\Delta z(K_k+\chi^0)}+\\ &+\frac{\frac{3\lambda_0^2}{8\pi}n\Delta z\big[\rho_{eg}(z+\Delta z,t)+\rho_{eg}(z,t)\big]}{1-i\frac{k_0}{4}\Delta z(K_k+\chi^0)}\,. \end{aligned} \tag{28}$$

With these scheme, we achieve second order precision in Δz. As one can see from eq. (28), the algorithm predicts $\Omega_k(z+\Delta z,t)$ if we know $\Omega_k(z,t)$ for all times t. This is fine for our purpose since we know the shape of the incoming field, in particular we initially assume a gaussian beam for all times t at $z=0$. Of course, everything said for eq. (21) is true for eq. (23). With the necessary modifications, one gets:

$$\Omega^{(-)}_{k,<}(z+\Delta z,t) = \frac{\Omega^{(-)}_{k,<}(z,t)\big[1-i\frac{k_0}{4}\Delta z(K_k+\chi^{0*})\big]+i\frac{k_0}{4}\chi^{(-)}\Delta z\big[\Omega^{(-)}_{k,>}(z+\Delta z,t)+\Omega^{(-)}_{k,>}(z,t))\big]}{1+i\frac{k_0}{4}\Delta z(K_k+\chi^{0*})}+ \\ + \frac{\frac{3\lambda_0^2}{8\pi}n\Gamma_{sp}\Delta z\big[\rho_{eg}(z+\Delta z,t)+\rho_{eg}(z,t)\big]}{1+i\frac{k_0}{4}\Delta z(K_k+\chi^0)} . \tag{29}$$

We observe that $\Omega^{(+)}_{k,>}$ and $\Omega^{(-)}_{k,<}$ are simply complex conjugate of one another.
For the partial differential equations of eqs. (22) and (24) we proced as follows. We first interpret the time derivative as a finite difference:

$$\frac{\partial\Omega^{(+)}_{k,<}(z,t)}{\partial t} \simeq \frac{\Omega^{(+)}_{k,<}(z,t+\Delta t)-\Omega^{(+)}_{k,<}(z,t)}{\Delta t} , \tag{30}$$

and we do the same for the spatial derivative. So, eq. (22) becomes:

$$\frac{\Omega^{(+)}_{k,<}(z,t+\Delta t)-\Omega^{(+)}_{k,<}(z,t)}{\Delta t} = \frac{c}{2}\Bigg[\frac{\Omega^{(+)}_{k,>}(z+\Delta z,t)-\Omega^{(+)}_{k,>}(z,t)}{\Delta z}+ \\ + i\frac{k_0}{2}\Big(K_k\Omega^{(+)}_{k,<}(z,t)+\chi^{(0)}\Omega^{(+)}_{k,<}(z,t)+\chi^{(+)}\Omega^{(+)}_{k,>}(z,t)\Big)+\frac{3\lambda_0^2}{8\pi}n\Gamma_{sp}\, d_{ge}\cdot\rho_{k,eg}(z,t)\Bigg] , \tag{31}$$

and one gets:

$$\Omega^{(+)}_{k,<}(z,t+\Delta t) = \Omega^{(+)}_{k,<}(z,t)+\overbrace{\Delta t\frac{c}{2}}^{=\Delta z}\Bigg[\frac{\Omega^{(+)}_{k,>}(z+\Delta z,t)-\Omega^{(+)}_{k,>}(z,t)}{\Delta z}+ \\ + i\frac{k_0}{2}\Big(K_k\Omega^{(+)}_{k,<}(z,t)+\chi^{(0)}\Omega^{(+)}_{k,<}(z,t)+\chi^{(+)}\Omega^{(+)}_{k,>}(z,t)\Big)+\frac{3\lambda_0^2}{8\pi}n\Gamma_{sp}\, d_{ge}\cdot\rho_{k,eg}(z,t)\Bigg] .$$

Using the equivalence $\frac{c}{2}\Delta t=\Delta z$ and evaluating the fields Ω and ρ at $z+\Delta z$, the scheme simplifies to:

$$\Longrightarrow \Omega^{(+)}_{k,<}(z,t+\Delta t) = \Omega^{(+)}_{k,<}(z+\Delta z,t)+\Delta z\Bigg[\frac{3\lambda_0^2}{8\pi}n\Gamma_{sp}\, d_{ge}\cdot\rho_{k,eg}(z+\Delta z,t)+ \\ i\frac{k_0}{2}\Big(K_k\Omega^{(+)}_{k,<}(z+\Delta z,t)+\chi^{(0)}\Omega^{(+)}_{k,<}(z+\Delta z,t)+\chi^{(+)}\Omega^{(+)}_{k,>}(z+\Delta z,t)\Big)\Bigg] . \tag{32}$$

As can be seen from eq. (33), to evolve the field from time t to time $t+\Delta t$ we need to know the field at time t and at position $z+\Delta z$. This is possible because, in our problem, we assume that the backward propagating wave is zero at time $t=0$ for every z, so at time $0+\Delta t$ we can safely use the algorithm. In fig. 7 we show a visual representation of how we are solving the problem, with the backward wave evolving from $(z+\Delta z,t)$ to $(z,t+\Delta t)$.

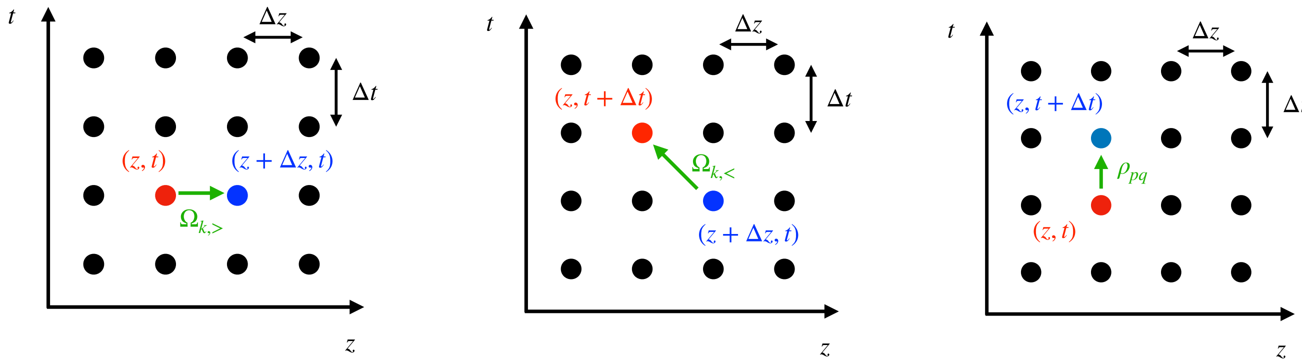

Figure 7: Schematic representation of the grid used for solving the propagation in time and space of the forward (left), the backward (center) propagating wave and the density matrix (left).

For $\Omega^{(-)}_{k,>}(z,t)$ we get:

$$\Omega^{(-)}_{k,>}(z,t+\Delta t) =\Omega^{(-)}_{k,>}(z+\Delta z,t) + \Delta z \Bigg[\frac{3\lambda_0^2}{8\pi} n\, d_{eg} \cdot \rho_{k,ge}(z+\Delta z,t) + \\ i\frac{k_0}{2}\Big(K_k \Omega^{(-)}_{k,>}(z+\Delta z,t) + \chi^{(0)*}\Omega^{(-)}_{k,>}(z+\Delta z,t) + \chi^{(+)*}\Omega^{(-)}_{k,<}(z+\Delta z,t)\Big)\Bigg]. \quad (33)$$

Regarding the Maxwell-Bloch equations (see eqs. (17), (18), (19) and (20)) a simple Euler scheme was used.

2.4 Results of the full simulation and comments

For the final simulation of light-matter interaction, we chose an initial field shaped like a Gaussian in space and time, of the form:

$$u(\mathbf{r},z,t) = u_0 \cdot \sqrt{\frac{1}{2\pi}\,\frac{e^{i\,\psi(z)}}{w(z)}}\; e^{-\frac{r^2}{2w(z)^2} - i\,k_0\,\frac{r^2}{2R(z)}}\; \frac{1}{\sqrt{2\pi\sigma_t^2}}\; e^{-\frac{(t-t0)^2}{2\sigma_t^2}}\,, \quad (34)$$

where the definitions of $\psi(z)$, $w(z)$ and $R(z)$ were given in section 1.2. Moreover, we set an initial population inversion of 1% at time $t=0$, i.e. we set $\rho_{ee}(r,z,t=0) = 0{,}01$ for all (r,z) points of the grid. In this way we expect the field to be amplified by the population inversion. For more information about the parameters of the beam, see section 2.5.
In this section we show the results of the simulation. In particular we show sections of the plane (r,z) for different times t in figs. 8, 9 and 10.
As we can see in figs. 8, 9 and 10, through the interaction with the field the coherences ρ_{eg} start to grow and lead to an increase in the intensity of the field, whose peak is dragged in time towards the end of the box. This evolution in time can be displayed in (z, ct) plots, which are shown in figs. 11, 12, 13 and 14.
If we focus our attention to the $r = 0{,}0$ plots (the top left ones) we see that the population inversion, which is present everywhere in space at time $t = 0$ (see fig. 14), causes an increase in the field intensity between times $t = 0$ and $t \simeq 2{,}5$. This increase of the field then results in a depopulation of the excited level. Then at time $t \simeq 5$ the intensity of the initial field start to grow, leading to

a peak of intensity, which is dragged to the end of the sample, as we can see in fig. 11. In the retarded time scheme that we are using, this results in a straight intensity peak at the centre of the box, which then fades due to absorbtion by the atoms. Finally, if we look at the density matrix elements in figs. 13 and 14 we see that they undergo Rabi oscillations in time, which means that the population levels oscillate in time due to the interaction with the field.

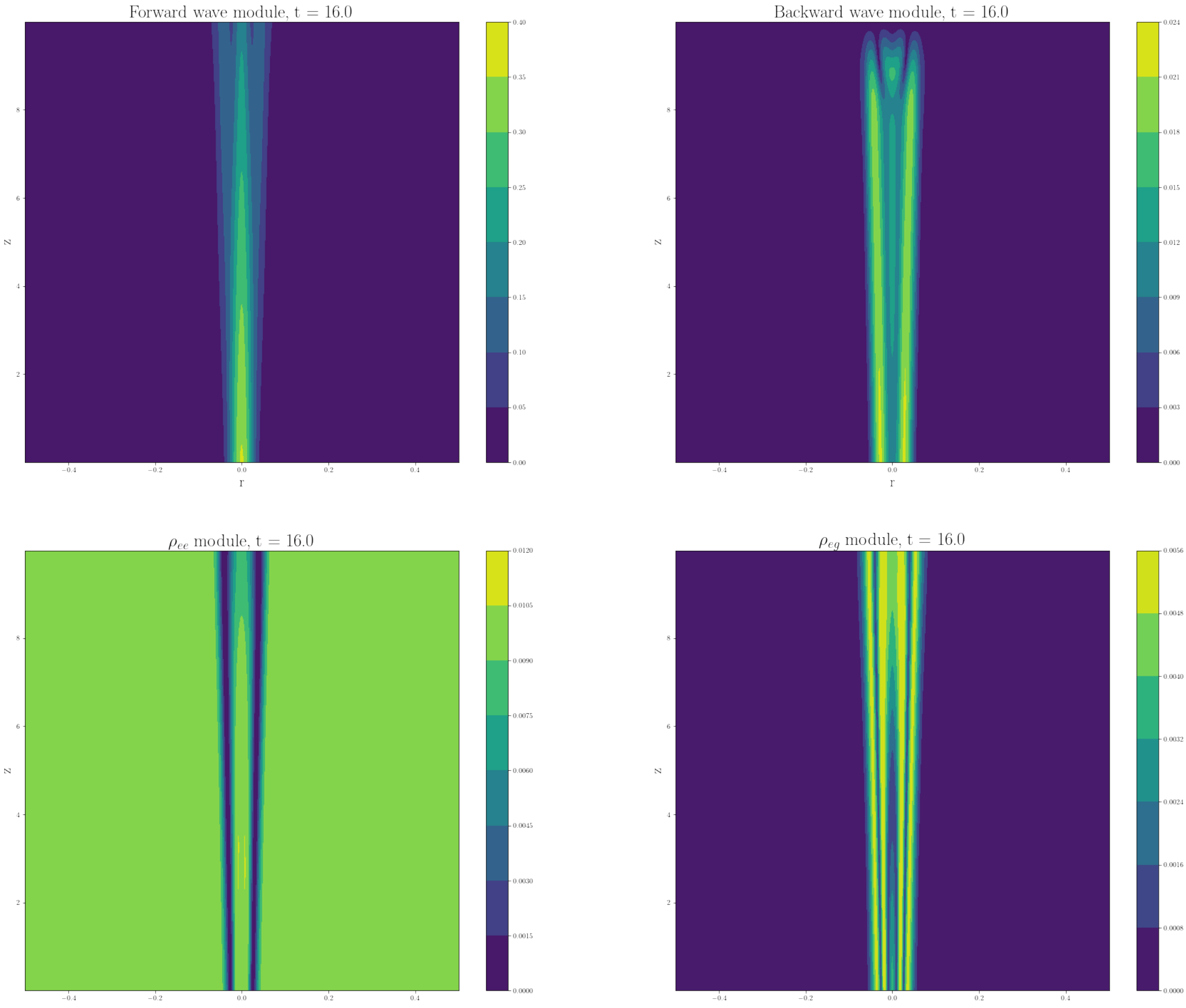

Figure 8: Representation in the (r, z) plane, at time $t = 16.0$ fs of: module of the forward propagating wave (top left), of the backward propagating wave (top right), of the density matrix elements ρ_{ee} (bottom left) and ρ_{eg} (bottom right).

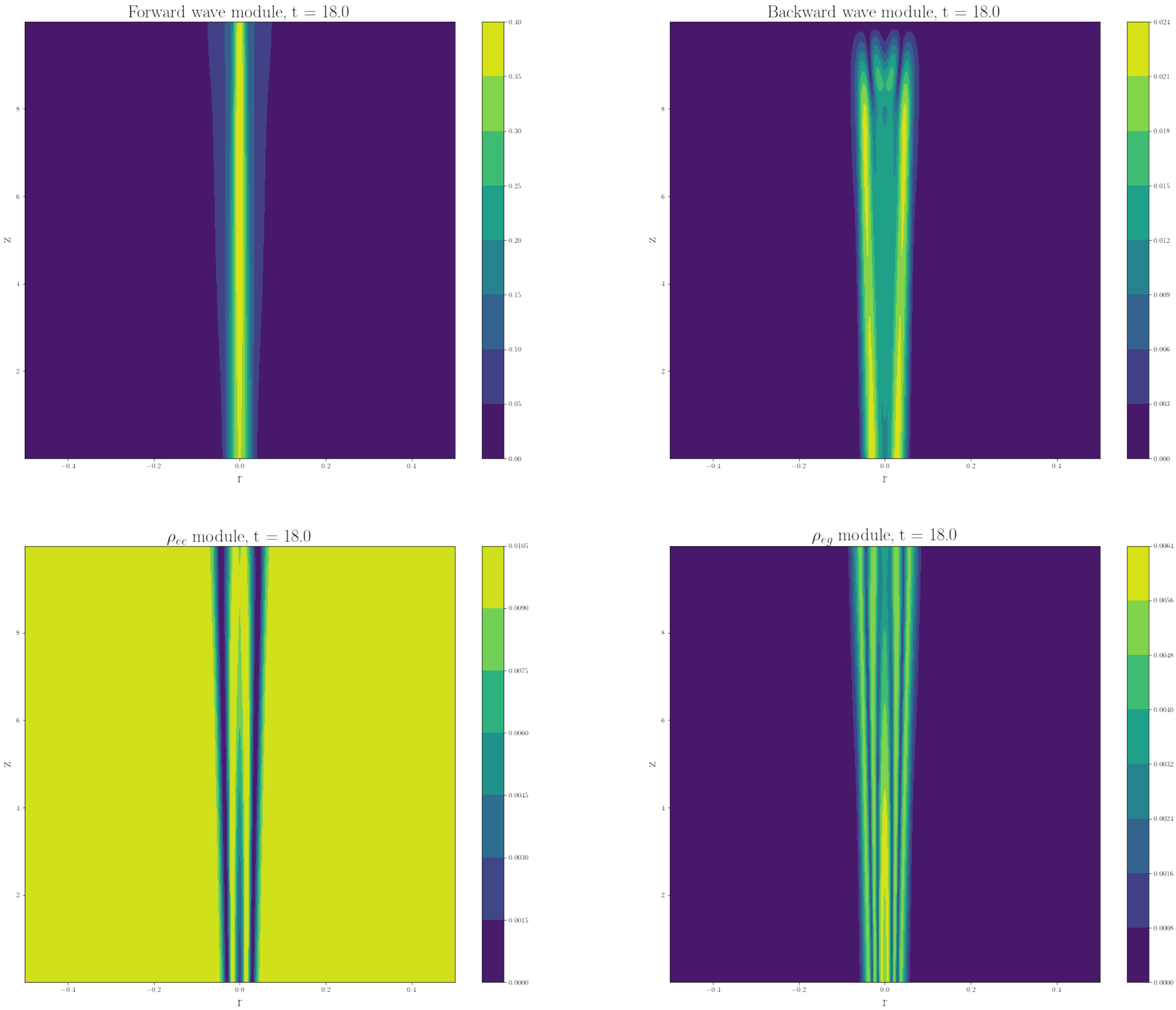

Figure 9: Representation in the (r, z) plane, at time $t = 18.0$ fs of: module of the forward propagating wave (top left), of the backward propagating wave (top right), of the density matrix elements ρ_{ee} (bottom left) and ρ_{eg} (bottom right).

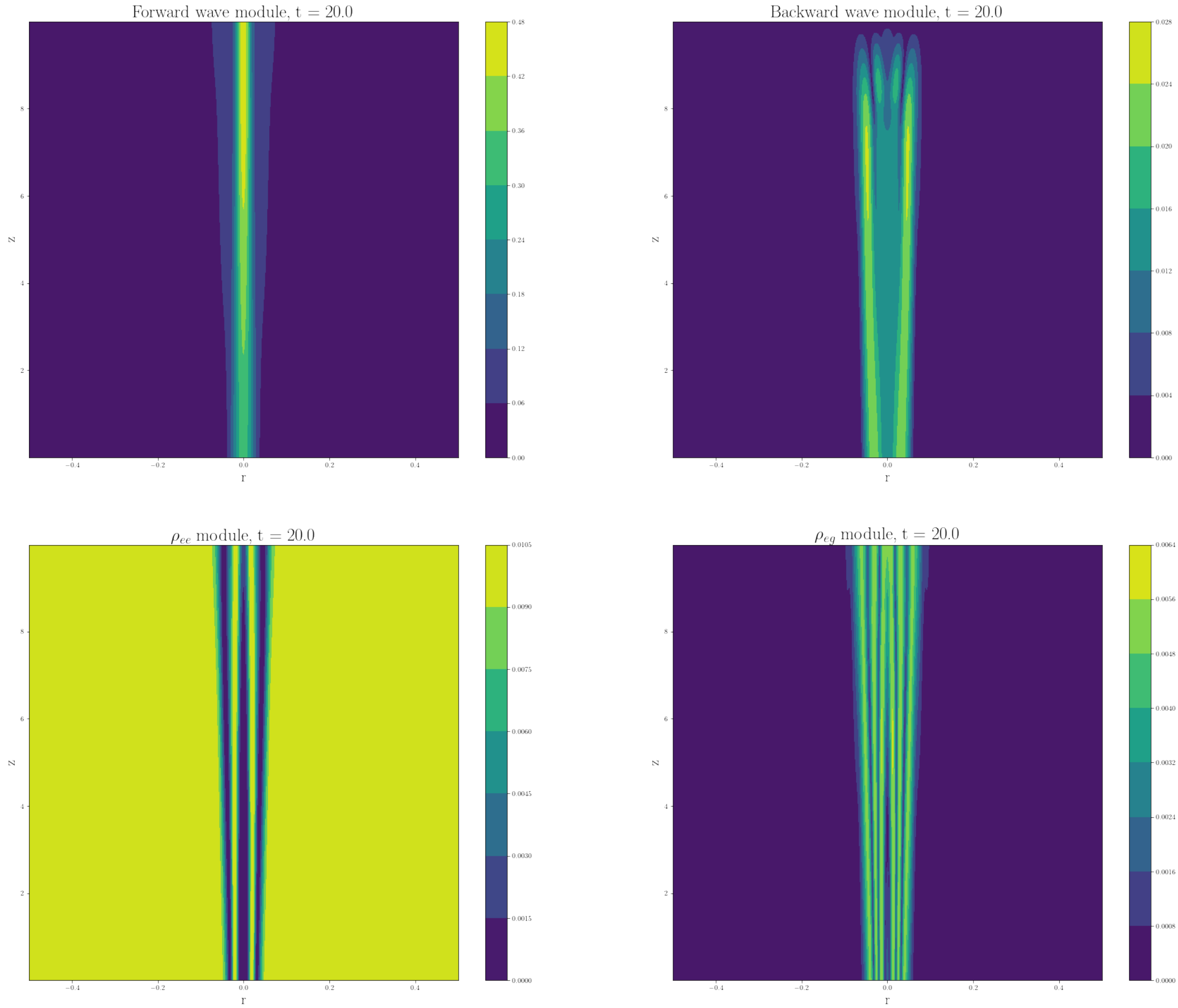

Figure 10: Representation in the (r, z) plane, at time $t = 20.0$ fs of: module of the forward propagating wave (top left), of the backward propagating wave (top right), of the density matrix elements ρ_{ee} (bottom left) and ρ_{eg} (bottom right).

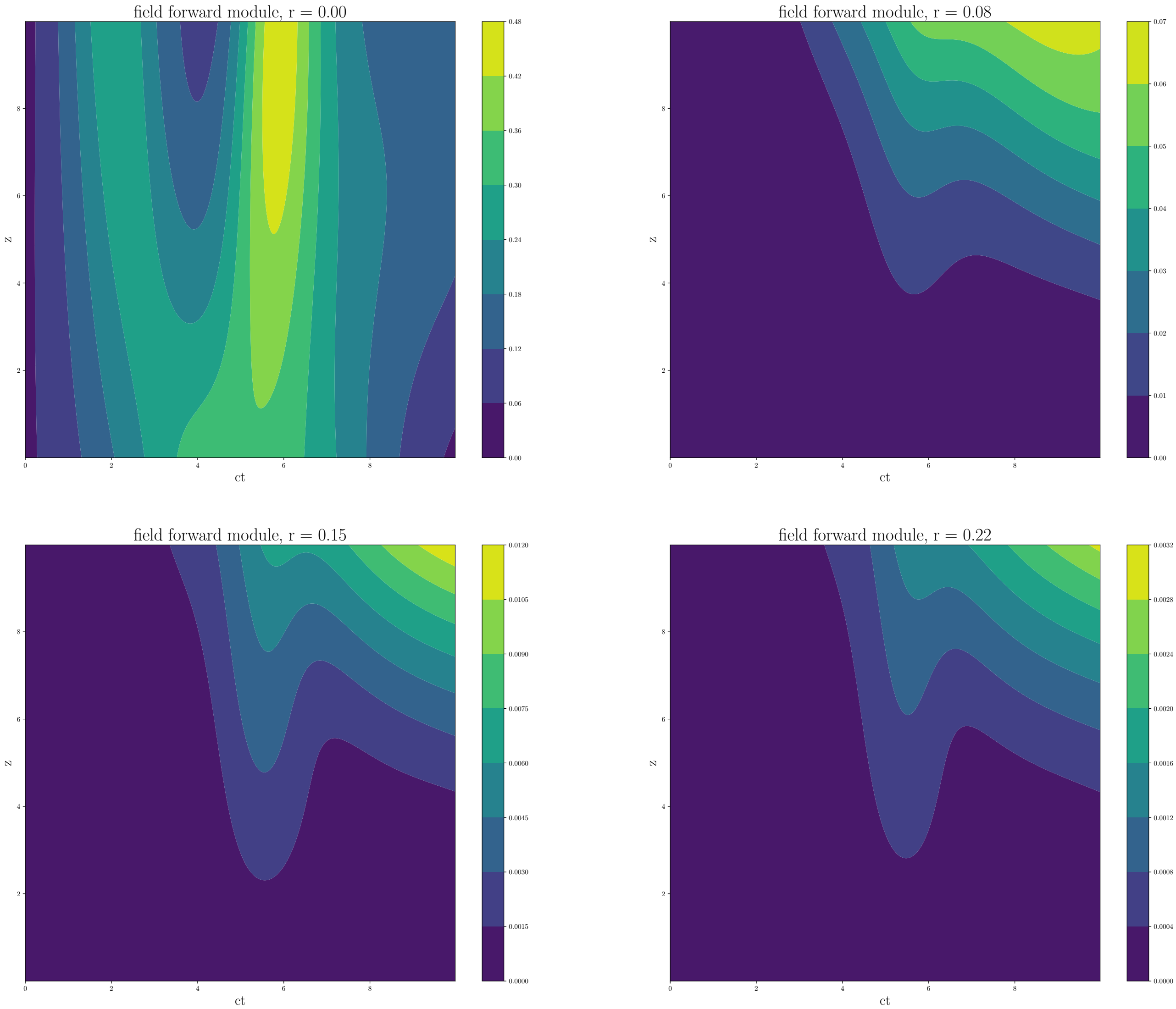

Figure 11: Representation in the (z,t) plane of the module of the **forward propagating wave** for: $r = 0.0\mu$m (top left), $r = 0.08\mu$m (top right), $r = 0.15\mu$m (bottom left) and $r = 0.22\mu$m (bottom right).

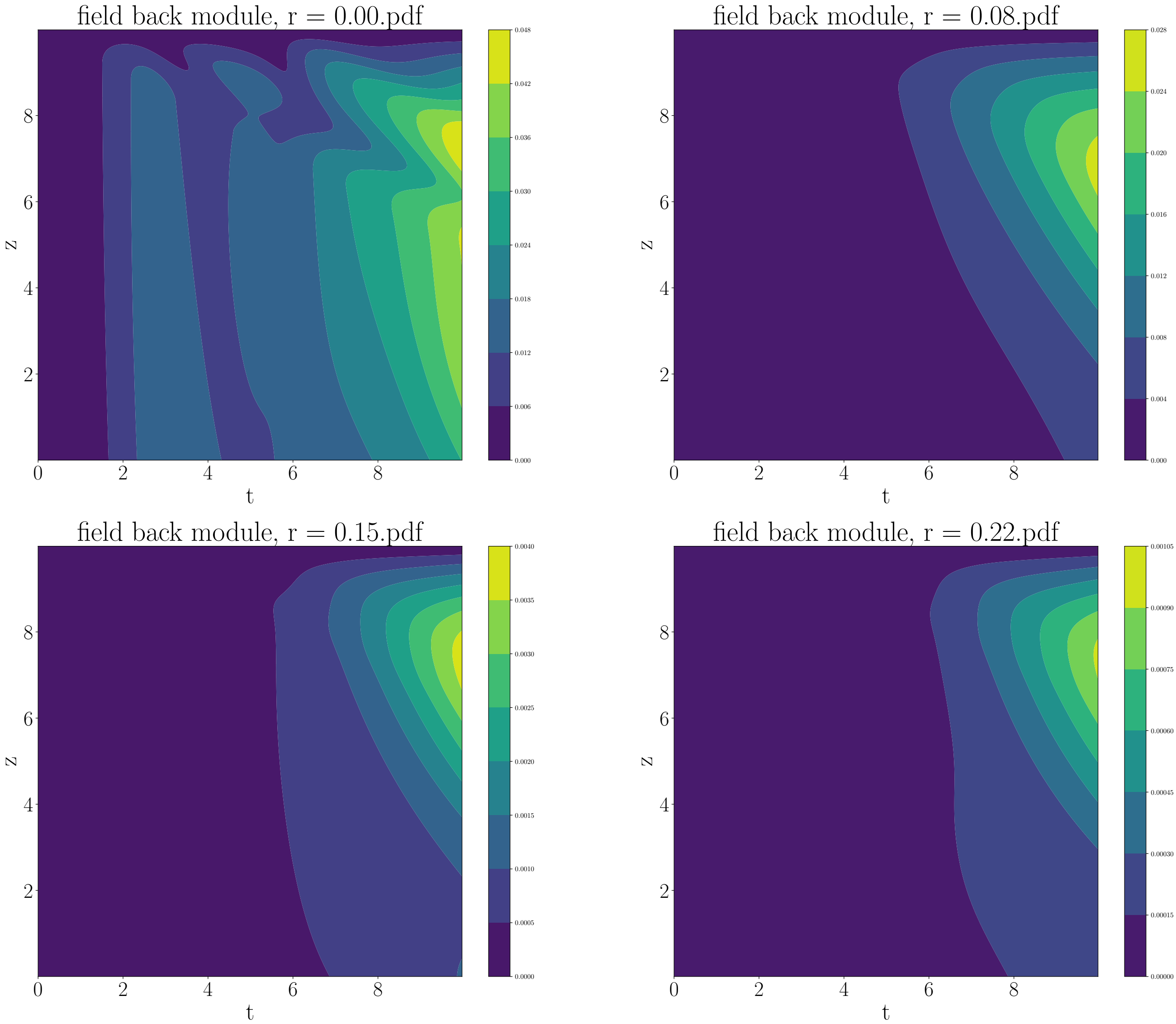

Figure 12: Representation in the (z, t) plane of the module of the **backward propagating wave** for: $r = 0.0\mu$m (top left), $r = 0.08\mu$m (top right), $r = 0.15\mu$m (bottom left) and $r = 0.22\mu$m (bottom right).

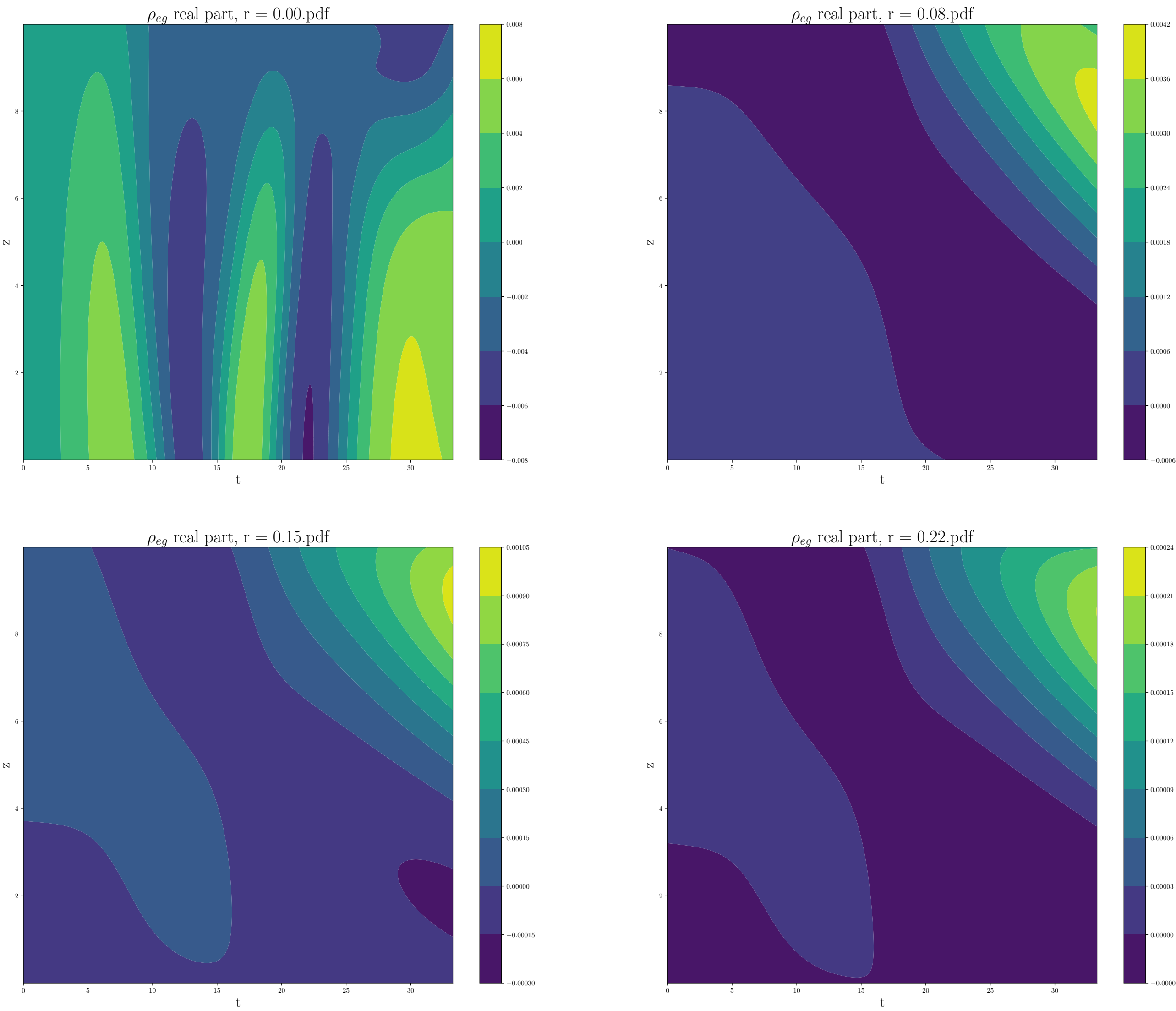

Figure 13: Representation in the (z, t) plane of the real part of the **coherences** $\rho_{eg}(r, z$ for: $r = 0.0\mu$m (top left), $r = 0.08\mu$m (top right), $r = 0.15\mu$m (bottom left) and $r = 0.22\mu$m (bottom right).

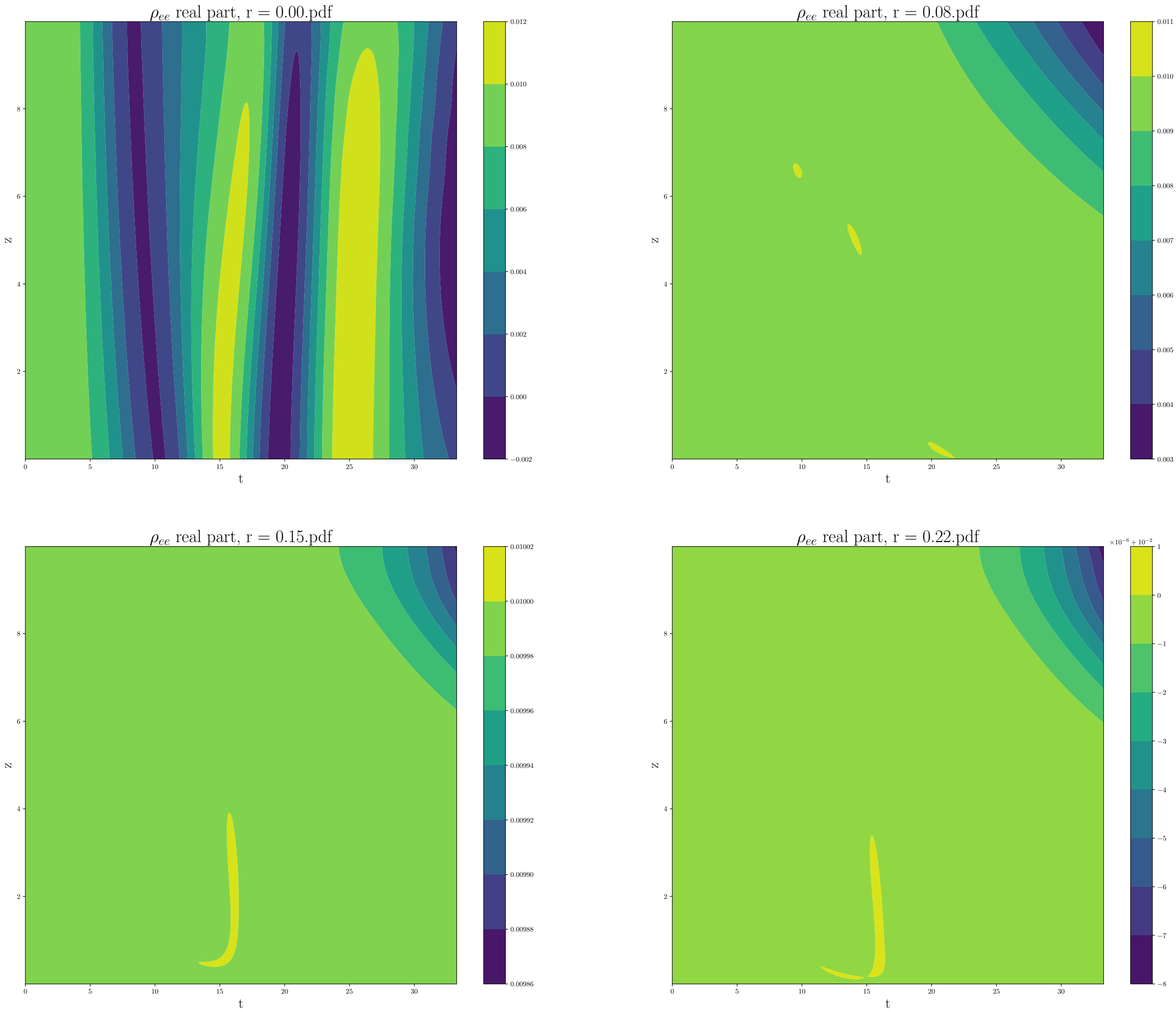

Figure 14: Representation in the (z,t) plane of the real part of the **population inversion** $\rho_{ee}(r,z$ for: $r = 0.0\mu$m (top left), $r = 0.08\mu$m (top right), $r = 0.15\mu$m (bottom left) and $r = 0.22\mu$m (bottom right).

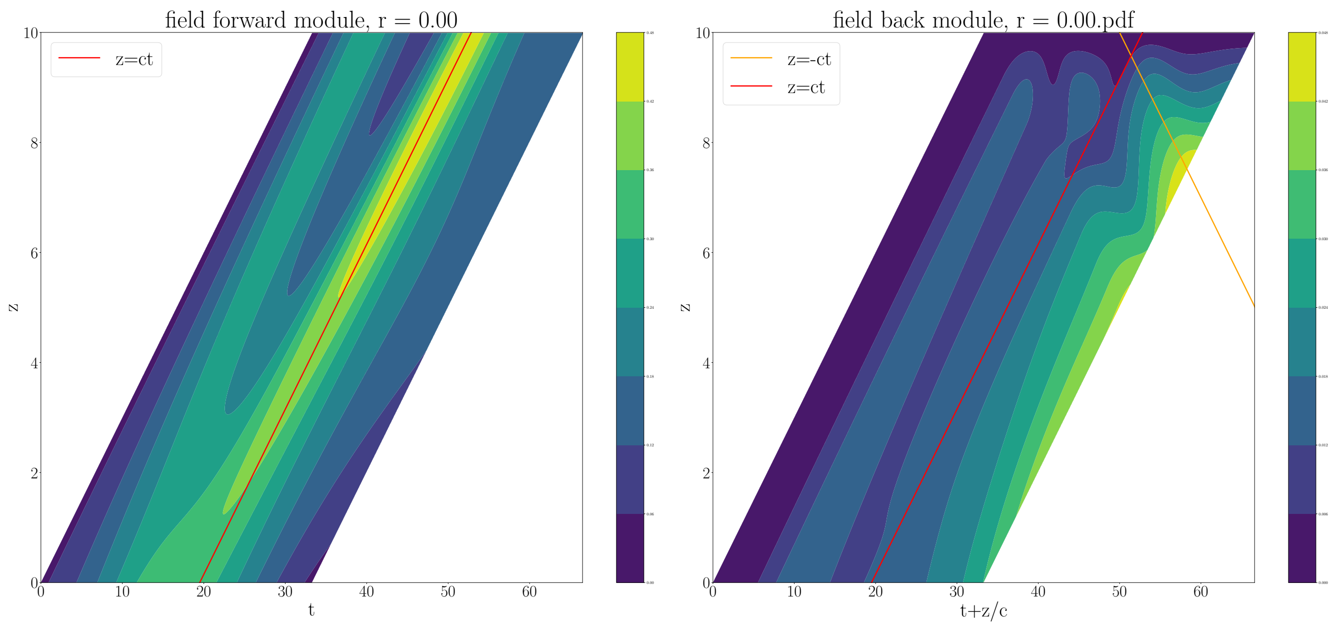

Figure 15: (z, t) plot of forward (left) and backward (right) propagating wave in the time reference of the laboratory. We add a red lines $z = \pm ct$ to show that the two waves propagate as they should.

As a final check, we plot the forward and backward wave evolution also in the time lab, to verify that they move accordingly to the law $z = ct$ and $z = -ct$ respectively. As one can see in **??**, the peaks of the forward propagating wave move along the $z = ct$ line, and those of the backward wave along the $z = -ct$ line. Moreover, one can see that the sources that generate the backward propagating wave are along the $z = ct$, since they are created by the forward propagating field.
Unfortunately, when using the algorithm for longer time the field and the density matrix elements grow indefinetely and after some time they lead to overflow, indicating some flaw in the method of the decomposition in Bessel functions, or in the algorithm itself. Moreover, the decomposition of the density matrix in Bessel functions becomes less and less accurate as time passes.

2.5 Parameters

Here we list the parameters used for the final simulations (showed in section 2.3):

- Width of the box: $R = 0,5\,\mu$m,
- Length of the box: $L = 10,0\,\mu$m,
- Time of the simulation: $T = 33,3$fs,
- Step of the grid in space: $\Delta z = 0,01\,\mu$m,
- Step of the grid in time: $\Delta t = 2/c\Delta z$,
- Initial beam intensity: $I_0 = 0,001\,\mu$J,
- Initial beam waist: $w_0 = 0,02\,\mu$m,
- Time of beam peak: $t_0 = 16,65$ fs,

- Width of beam in time: $\sigma_t = 8,325$ fs,
- Beam wavelenght: $\lambda_0 = 1,54\,\mathring{A}$,
- Number of Bessel functions: $n_{Bessel} = 25$,
- Spontaneous decay constant: $\Gamma_{sp} = 1/(0,92)$ fs^{-1},
- Atomic density: $n = 1,0$ nm^{-3},
- Susceptibility: $\chi^{(0)} = (-37.3763 + 1.66806\,i)\,10^{-7}$
- Susceptibility: $\chi^{(+)} = (-6.97952 + 5.07316\,i)\,10^{-7}$
- Susceptibility: $\chi^{(-)} = (-7.70248 - 4.20542\,i)\,10^{-7}$
- Initial population inversion: $\rho_{ee}(t = 0) = 0,01$

3 Conclusions and future developments

In conclusion, the code gives correct results in terms of the propagation of the beam. The predictions have been cross-checked multiple times both with known analytics and with another code. Regarding the light-matter interaction part, the results of the simulations are coherent and trustworthy, and show all the features that we were looking for, in particular the amplification of the field intensity. However, the code fails for long simulation times (more than $\simeq 40$ fs), so this should raise some concern about the stability of the algorithm. One suggestion for the future could be to try and implement a more stable numerical scheme. Moreover, to get a more complete and realistic simulation it would be appropriate to implement a pump-probe scheme in which an initial beam acts as a pump and creates a population inversion, which is then probed by the Gaussian field that was implemented in the code.

References

[1] Theodore H Maiman et al. Stimulated optical radiation in ruby. 1960.

[2] W al Ackermann, G Asova, V Ayvazyan, A Azima, N Baboi, J Bähr, V Balandin, B Beutner, A Brandt, A Bolzmann, et al. Operation of a free-electron laser from the extreme ultraviolet to the water window. *Nature photonics*, 1(6):336–342, 2007.

[3] Paul Emma, R Akre, J Arthur, R Bionta, C Bostedt, J Bozek, A Brachmann, P Bucksbaum, Ryan Coffee, F-J Decker, et al. First lasing and operation of an ångstrom-wavelength free-electron laser. *nature photonics*, 4(9):641–647, 2010.

[4] Tetsuya Ishikawa, Hideki Aoyagi, Takao Asaka, Yoshihiro Asano, Noriyoshi Azumi, Teruhiko Bizen, Hiroyasu Ego, Kenji Fukami, Toru Fukui, Yukito Furukawa, et al. A compact x-ray free-electron laser emitting in the sub-ångström region. *nature photonics*, 6(8):540–544, 2012.

[5] Linda Young. A stable narrow-band x-ray laser. *Nature*, 524(7566):424–425, 2015.

[6] Hitoki Yoneda, Yuichi Inubushi, Kazunori Nagamine, Yurina Michine, Haruhiko Ohashi, Hirokatsu Yumoto, Kazuto Yamauchi, Hidekazu Mimura, Hikaru Kitamura, Tetsuo Katayama, et al. Atomic inner-shell laser at 1.5-ångström wavelength pumped by an x-ray free-electron laser. *Nature*, 524(7566):446–449, 2015.

[7] Nina Rohringer, Duncan Ryan, Richard A London, Michael Purvis, Felicie Albert, James Dunn, John D Bozek, Christoph Bostedt, Alexander Graf, Randal Hill, et al. Atomic inner-shell x-ray laser at 1.46 nanometres pumped by an x-ray free-electron laser. *Nature*, 481(7382):488–491, 2012.

[8] Anthony E Siegman. *Lasers*. University science books, 1986.

[9] Robert W Boyd. *Nonlinear optics*. Academic press, 2020.